Materials Transactions, Vol. 49, No. 2 (2008) pp. 352 to 359

Low Temperature Isothermal Reduction Kinetics of Fe_2O_3/NiO Mixed Oxides and Comparative Synthesis of $Fe_{1-x}Ni_x$ Alloys

Jong-Jin Pak, M. Bahgat*[1], Bo-Ho Kim*[2] and Min-Kyu Paek*[2]

Department of Metallurgical and Materials Eng., Hanyang University, Ansan 426-791, Korea

Two Molar ratios 1 : 1 and 1 : 2 of AR grade nickel oxide and iron oxide powder was mixed and compacted. The fired compacts were isothermally reduced in pure hydrogen at 500, 550, 600 and 650°C. Based on thermogravimetric analysis, the reduction behavior and kinetics reaction mechanism were studied comparatively for the different mixed oxides ratios. The initial fired powder and the various reduction products were characterized by XRD, SEM, TEM and reflected light microscope to reveal the effect of hydrogen reduction on composition and microstructure of produced Ferronickel alloy. Synthesis of nanocrystalline $Fe_{1-x}Ni_x$ alloy with 33 and 20 at% Ni for reduction of 1 : 1 and 1 : 2 NiO/Fe_2O_3 ratios was detected respectively. The activation energy values were calculated from Arrhenius equation and the approved mathematical formulations for the gas solid reaction were applied. It was found that for NiO/Fe_2O_3 of both 1 : 1 and 1 : 2 ratios, the initial reduction stages is controlled by the combined gaseous diffusion and interfacial chemical reaction mechanisms while at the final reduction stages the reaction is controlled by the interfacial chemical reaction mechanism. [doi:10.2320/matertrans.MRA2007203]

(Received August 20, 2007; Accepted November 12, 2007; Published December 19, 2007)

Keywords: *Fe_2O_3/NiO, H_2-reduction, nanocrystallites, iron-nickel alloy, fcc-alloy, bcc-alloy*

1. Introuduction

There is considerable technological and theoretical interest in magnetic nanoparticles because properties such as magnetic recording density, recording speed, the noise suppression, and the material lifetime are remarkably enhanced with the decrease in magnetic particle size.[1)] Transition metal alloys and compounds have been studied extensively in the past several decades for their increasing utility in electronic and energy conversion devices.[2)] As important transition metal alloys, iron-nickel alloys are of great interest due to their low thermal expansion[3)] and their remarked magnetic properties.[4–6)] These materials are important for applications as well as for fabrication. Fabrication and structure of Fe-Ni alloy were studied by some investigators.[7–11)]

Slight variation of the composition in the Fe–Ni alloy can cause substantial changes in the coercive, anisotropic and magnetostrictive properties.[12)] An important feature of the Fe-Ni alloy system is its structural evolution, with a change from bcc for the Fe-rich alloy to fcc for the alloy with larger Ni content.[13)] Jartych *et al.*[14)] found that in the case of Fe-Ni alloys the bcc solid solution was formed during high-energy ball milling for the composition with 20 at% Ni, while around 35 at% Ni the fcc solid solutions were obtained. Also Qiang *et al.* concluded that for $Fe_{1-x}Ni_x$ when $x = 0.25$, fcc and bcc structure coexist obviously, while when $x = 0.50$, 0.75, most of $Fe_{1-x}Ni_x$ alloy nanoparticles have fcc structure.[15)]

Fe–Ni alloys with concentration of around 35 at% Ni and fcc crystal lattice structure, which are called "invar alloys", show various anomalies in mechanical and magnetic properties such as an extraordinary low thermal expansion coefficient, the deviation of the spontaneous magnetization from the Slater–Pauling curve, the strong negative pressure dependence of the Curie temperature, TC, and so on.[16)] While for 20%Ni and bcc crystal lattice structure, it is called permalloy ($Ni_{20}Fe_{80}$), which is the most common magnetic material used in microelectromechanical systems (MEMS) application.

Iron-nickel alloy ultrafine particles can be prepared by a number of methods such as the mechanical attrition of elemental powders,[17)] the levitation melting technique in a cryogenic environment of liquid nitrogen,[18)] and electrodeposition in a flow cell.[19)] Also as ceramic route synthesis of nanosized Ni-Fe powder by hydrogen reduction of mixed NiO-Fe_2O_3 was investigated. Lee *et al.*[20)] found that the alloying of Ni-Fe during reduction of NiO-Fe_2O_3 powder was enhanced in the ball milled oxide mixture. Such rapid alloying process yielded the stable Ni-Fe alloy aggregates consisting of 20–70 nm nanosized alloy particles. The chemical homogeneity with large surface area during reduction process is believed to be responsible for the formation of nanoalloy powder. Actually the reaction kinetics and mechanisms is very important to clarify the reaction rate and controlling reaction mechanism but unfortunately it is not covered well in these nanoscale studies. At the same time, Bahgat *et al.*,[21)] studied the reduction kinetics of co-precipitated nickel ferrite from secondary resources, in pure hydrogen at 800–1100°C. FCC Fe-Ni alloy ($Fe_{0.64}Ni_{0.36}$) was formed with crystalline size ranged from 78 to 98 nm. Grain growth and coalescence of the formed alloy grains took place by increasing the reduction temperature.

In the present work, the low temperature reduction kinetics and mechanism of Fe_2O_3/NiO mixture with synthesis of $Fe_{1-x}Ni_x$ (20 and 33 at% Ni) alloys nanoparticles was investigated.

2. Experimental

Molar ratios 1 : 1 and 1 : 2 of very fine (1 μm) analytical reagent grade (99.9%) nickel oxide and ferric oxide were well mixed in agate mortar and by dry ball milling for 6 h.

*[1]Researcher, Minerals Technology Department, Central Metallurgical Research and Development Institute (CMRDI), Cairo, Egypt.
*[2]Graduate Student, Hanyang University

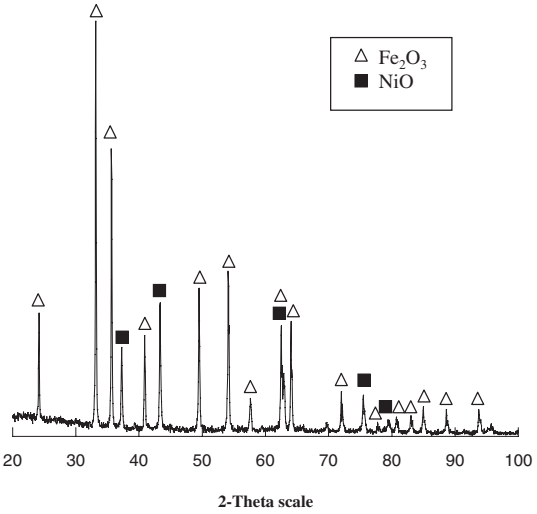

Fig. 1 XRD pattern of $NiO/2Fe_2O_3$ mixture compact fired at 500°C.

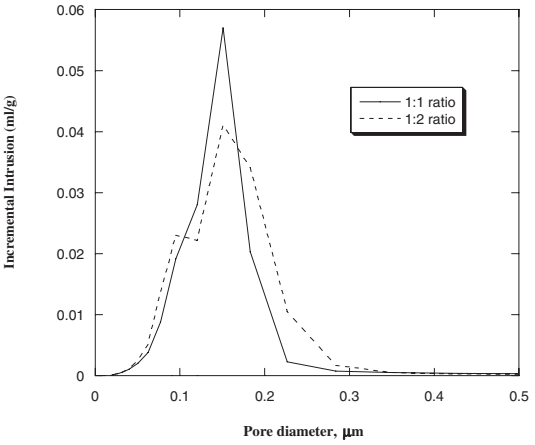

Fig. 2 The relation between incremental pore volume and pore diameter for 1 : 1 and 1 : 2 ratio of NiO/Fe_2O_3 fired briquettes.

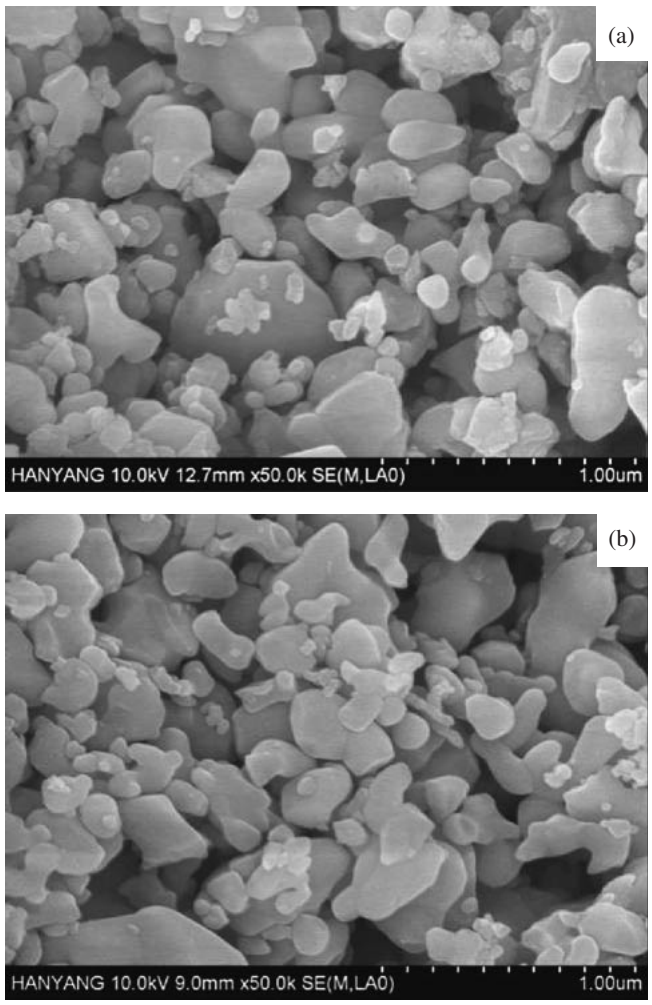

Fig. 3 SEM micrograph of fired NiO/Fe_2O_3 compact at 500°C (a) 1 : 1 and (b) 1 : 2 molar ratios.

Equal weights of mixed powders were compressed into compacts of about 1.5 g weight, 7 mm diameter and 3 mm thickness. The prepared compacts were dried at 105°C for 24 hrs and then fired at 500°C for 1 hr then cooled to room temperature gradually.

The fired compacts were reduced at 500, 550, 600 and 650°C in constant flowing hydrogen gas atmosphere (100% H_2). Partial reduction (25 and 80%) was also applied for confirmation of reduction mechanism. The course of reduction was followed up thermogravimetrically by means of a weight loss method using an automatic sensitive balance equipped with the vertical tube furnace.

The reduction extent is calculated as follow;

$$\%\text{reduction} = ([\text{weight of } O_2 \text{ removed at a given time}] / [\text{weight of } O_2 \text{ in NiO-}Fe_2O_3] \times 100).$$

So the reduction extent was correlated to the total removable oxygen of both nickel and iron oxides.

A gas purification system was used to obtain 99.99% purity hydrogen gas. The reduction assembly and gas flow system used in this study were previously mentioned.[22] The fired powder and the reduced products were identified and characterized by X-ray phase analysis technique (XRD, High power X-ray Diffractometer System, Rigaku D/MAX-2500/PC) with Cu Kα_1 radiation ($k = 0.154056$ nm) at a scanning rate of $0.067^\circ\,s^{-1}$ in the 2θ range from 10° to 80°. High Resolution Field Emission scanning electron microscope (FE-SEM, Hitachi S4800), energy dispersive X-ray spectrometry (EDX-Hitachi S4800), optical microscope (Olympus PMG3), transmission electron microscope (TEM-JEOL-3010) and Auto-Pore IV 9500 V1.06 (MICROMERITICS INSTRUMENT CO.).

In each experiment, after the furnace was heated up to the required temperature the fired compact was put inside a basket to be hanged in the balance and adjusted in the middle zone of the tube furnace in flow of purified Ar gas. After settling down for about 10–15 min for the sample to acquire the given temperature, the reducing gas was passed while the Ar gas was stopped. The reacted compact was kept in the reducing atmosphere till a constant weight was achieved. For cooling, the reducing gas was replaced by Ar and the reduced sample was pulled up at the upper part of the reaction tube and kept away from the hot zone. After the temperature became below 200°C, the reduced compact was quenched in pure acetone.

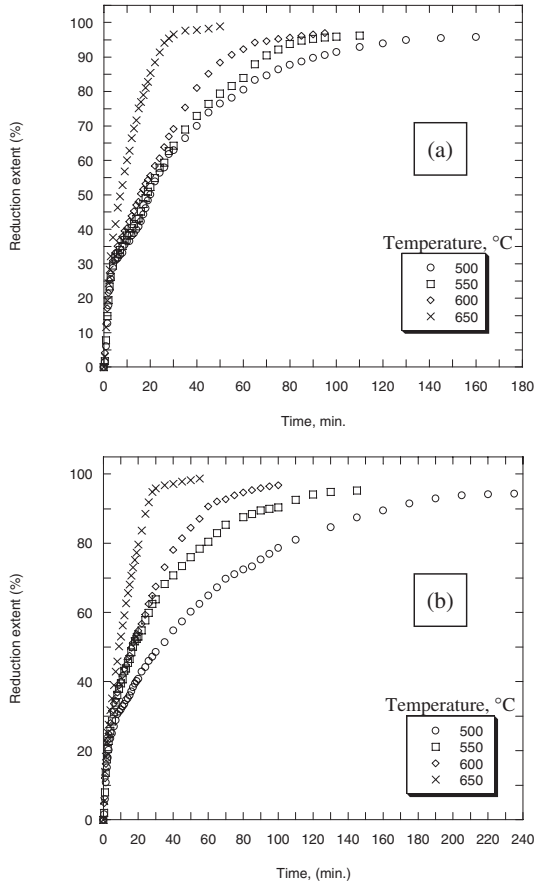

Fig. 4 Reduction curves of fired NiO/Fe_2O_3 compacts reduced at 500–650°C with pure hydrogen gas. (a) 1 : 1 and (b) 1 : 2 molar ratios.

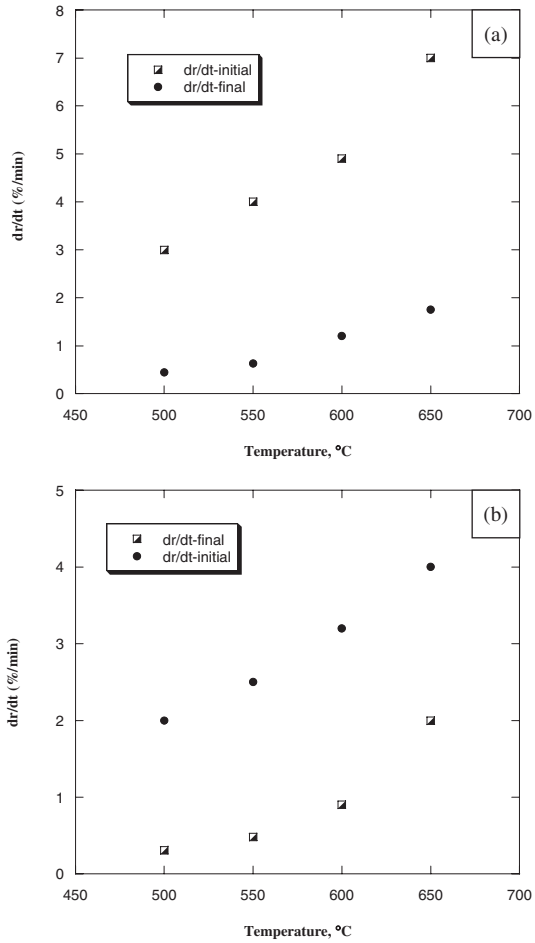

Fig. 5 Effect of reduction temperature on the reduction rate of (a) 1 : 1 and b) 1 : 2 NiO/Fe_2O_3 at the initial and final reaction stages.

3. Results and Discussion

3.1 Characterization of the fired compacts

The two different ratios (1 : 1 and 1 : 2) of mixed NiO and Fe_2O_3 powder were fired at 500°C for 1 h and then cooled gradually. Figure 1 shows the XRD pattern of $NiO/2Fe_2O_3$ mixed oxide powder after firing. Only the NiO and Fe_2O_3 diffraction peaks are clearly detected as pure phases that reflected the absence of any new phase formation due to firing at this temperature.

The average crystallite size of the fired mixed oxides powder was 44.4 and 52 nm for 1 : 1 and 1 : 2 ratios respectively as calculated from X-ray analysis based on the full-width at half-maximum (FWHM) of the diffraction peak using the following Scherer's formula,[20)]

$$D = 0.9\lambda/(\beta - \beta 1)\cos\theta$$

Where D is the crystallite size, λ the X-ray wave length, β the broadening of the diffraction peak and θ is the diffraction angle.

The pore size measurements show that both samples have nearly the same total porosity values (44.82% and 46.0% for 1 : 1 and 1 : 2 ratio samples respectively). The measured pore size distributions are shown in Fig. 2. It can be seen that both samples showed the same pore size distribution but the total pore volume decreased slightly by presence of higher ratio of Fe_2O_3.

The SEM examination for nanocrystalline powder of fired NiO and Fe_2O_3 oxides mixture in 1 : 1 and 1 : 2 ratios is shown in Fig. 3(a) and (b) respectively. Similar morphology was observed for both samples whereas the powder grains of the fired oxides mixtures have irregular crystalline shape. These grains are homogeneously distributed in the size range of 100–500 nm in a relatively highly porous structure with absence of any clustering, coalescence or sintering effect.

3.2 Reduction behavior and morphological aspects

Fired NiO/Fe_2O_3 and $NiO/2Fe_2O_3$ compacts were isothermally reduced with pure H_2 gas at different temperatures ranging from 500 to 650°C. The isothermal reduction curves for the two ratios are shown in Fig. 4(a) and (b). Similar trends were observed during reduction of both ratios. It can be seen that for each reduction curve, the rate of reduction was highest at early stage and gradually decreased with time till the end of experiment. The reduction rate increased as the reduction temperature increased either in the initial or final reaction stages. Also it is observed that almost complete reduction was achieved at all the reaction temperatures whereas the reduction extents were ranged from about 96–100% for both NiO/Fe_2O_3 and $NiO/2Fe_2O_3$ compacts. The reaction time decreased gradually with increasing the reduction temperatures from 500 to 650°C whereas it decreased from 160 to 50 min during reduction of 1 : 1 ratio compacts (Fig. 4(a)) while it decreased from 235 to 55 min

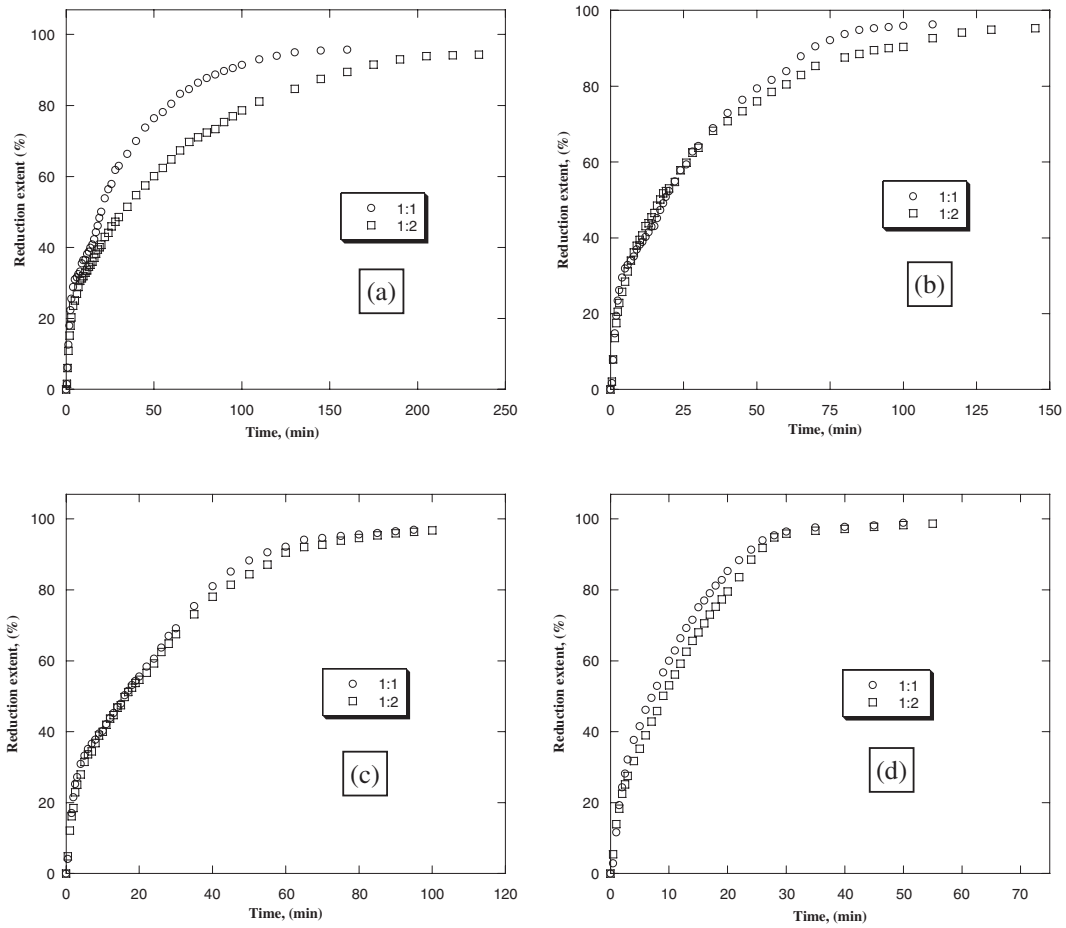

Fig. 6 Reduction rate of 1 : 1 and 1 : 2 NiO/Fe_2O_3 samples at (a) 500, (b) 550, (c) 600 and (d) 650°C.

during reduction of 1 : 2 ratio compacts (Fig. 4(b)) respectively. The correlation between the reduction rate (dr/dt) at both initial (0–25% reduction extent) and final (60–85% reduction extent) stages and the reduction temperature are shown in Fig. 5 a and b for NiO/Fe_2O_3 and $NiO/2Fe_2O_3$ respectively. These Figures are clarifying the increasing of the reduction rate with increasing the reduction temperature at both initial and final stages.

Comparatively, it was observed that reduction rate of NiO/Fe_2O_3 compacts was faster with shorter reaction time than $NiO/2Fe_2O_3$ compacts especially at lower temperatures and these differences decreased sharply with increasing reduction temperatures as shown in Fig. 6(a)–(d). This is owing to the higher oxygen contents in $NiO/2Fe_2O_3$ samples relative to NiO/Fe_2O_3 one and also might be owing to the slightly higher total pore volume in NiO/Fe_2O_3 samples relative to $NiO/2Fe_2O_3$ one (Fig. 2). So with increasing the reaction temperatures the oxygen removal rate will be faster to minimize the effect of the above mentioned factors and decreasing this difference in the reaction rate.

Figures 7(a), (b) and 8(a), (b) shows the X-ray diffraction analyses of the reduced NiO/Fe_2O_3 and $NiO/2Fe_2O_3$ samples at different temperatures. It was found that either at lower or higher reduction temperatures, the only detected phases were the Fe-Ni alloys that mean the different mixed oxides ratios were almost reduced completely with the formation of ferro-nickel alloy. It was observed that the peaks of the synthesized $Fe_{1-x}Ni_x$ alloy are strong and sharp revealing the high crystallinity of the nanoparticles.

The average crystallite sizes of the synthesized $Fe_{1-x}Ni_x$ alloys produced from NiO/Fe_2O_3 reduction were 13 and 34 nm while that produced from $NiO/2Fe_2O_3$ were 14 and 33 nm. Through analysis of the diffraction peaks at different 2θ values depending on JCPDS analysis. It was found that reduction NiO/Fe_2O_3 leads to mixture of fcc and bcc-lattice of Fe-Ni alloy while the reduction of NiO/Fe_2O_3 leads to mainly bcc alloy with traces of fcc alloy.

The EDX quantitative analysis for the reduced product at 650°C is shown in Fig. 9(a) and (b). It is found that after reduction of NiO/Fe_2O_3 the Ni content in the synthesized $Fe_{1-x}Ni_x$ alloy is 33.1 at% and 34.3 mass% while after reduction of $NiO/2Fe_2O_3$ the Ni content in the $Fe_{1-x}Ni_x$ alloy is 20.1 at% and 21.2 mass%.

Morphological observation of reduced NiO/Fe_2O_3 and $NiO/2Fe_2O_3$ compacts at different temperatures using SEM is shown in Fig. 10(a)–(d). Generally it can be seen that the Fe-Ni alloy are formed in irregular crystalline shape grains of different size with presence of micro- and macro-pores. Also it was observed that with increasing the reduction temperature grain growth and slightly coalescence with sintering effect was detected in a less porous structure. The TEM examination is also handled for the synthesized nanocrystalline Fe-Ni as shown in Fig. 11 for the reduced $NiO/2Fe_2O_3$ samples. It was observed that the Fe-Ni alloy particles were

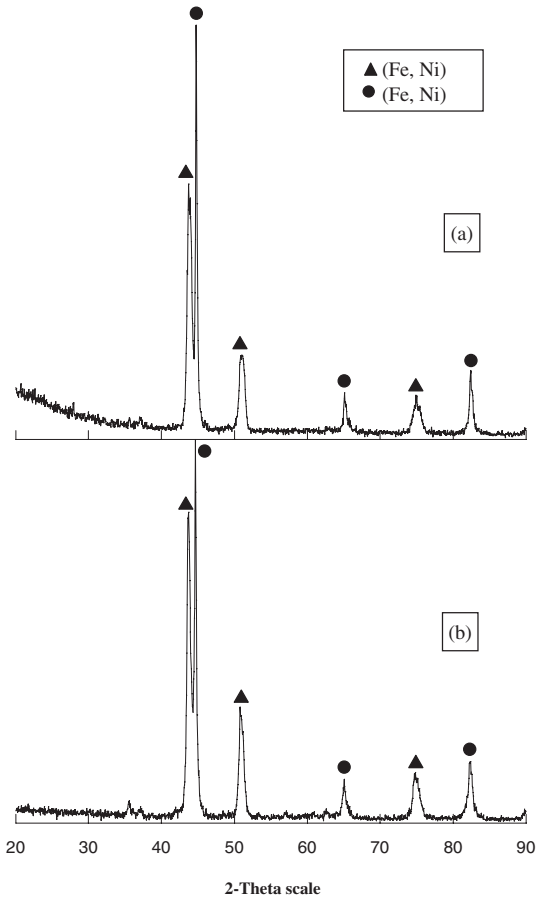

Fig. 7 XRD pattern of synthesized Fe-Ni alloy after complete reduction of 1 : 1 NiO/Fe_2O_3 at (a) 650 and (b) 500°C.

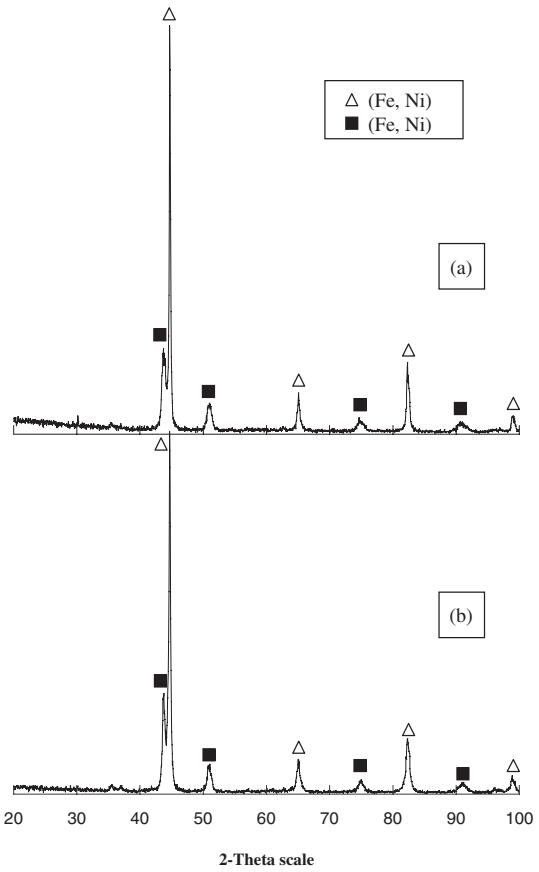

Fig. 8 XRD pattern of synthesized Fe-Ni alloy after complete reduction of 1 : 2 NiO/Fe_2O_3 at (a) 650 and (b) 550°C.

formed with average size about 20 nm in presence of agglomeration effect.

3.3 Reduction kinetics and mechanisms

Partial reduction of NiO/Fe_2O_3 and $NiO/2Fe_2O_3$ compacts was carried out to 25 and 80% reduction extent to clarify the reduction progressing and mechanism investigating. XRD analysis for partially reduced NiO/Fe_2O_3 samples to 80 and 25% reduction extent at 600°C is shown in Fig. 12(a) and (b) respectively. It is found as the reduction proceeded under the strong reducing effect of the H_2 gas, the oxygen removal successfully takes place on the oxide phases to the gradual observation of lower iron oxides (Fe_3O_4, FeO) then metallic Ni and Fe and final formation of Fe-Ni alloy.

The apparent activation energy (*Ea*) of reduction was calculated at both the initial and the final reaction stages to illustrate the rate controlling mechanism depending on Arrhenius equation,;

$$K_r = K_o e^{-Ea/R_g T} \quad (1)$$

where K_r is the rate constant, K_o is the frequency factor, R_g is the gas constant and T is the absolute temperature. The reaction rate constant (K_r) can be derived from a rate equation of the form:

$$dr/dt = K_r P^n \quad (2)$$

where P^n is the pressure of the reducing gas and n is the order of reaction. The relationships between the logarithm of the rate of reduction and the reciprocal of the absolute temperature are plotted at both the initial and latter stages for NiO/Fe_2O_3 and $NiO/2Fe_2O_3$ as shown in Fig. 13(a) and (b) respectively. For 1 : 1 NiO/Fe_2O_3, the calculated values of the apparent activation energy obtained from these relationships at the initial and final reaction stages are 35.82 and 57.32 kJ/mole respectively. At the same time the calculated values of the apparent activation energy at the initial and final reduction stages of 1 : 2 NiO/Fe_2O_3 are 26.27 and 72.6 kJ/mole respectively.

The apparent activation energy value is a well known criteria to show to what extent the reaction is feasible and it has been calculated by many investigators in order to determine the rate controlling step as shown in Table 1.[23] The calculated activation energy values indicate that for the two different mixed oxides ratios, the reduction process at the initial reaction stages is controlled by the combined gas diffusion and interfacial chemical reaction mechanisms while the final reaction stages is controlled by the interfacial chemical reaction mechanism.

However, the mechanisms based on the magnitude of activation energy are not decisive but rather indicative.[24] Accordingly, in order to confirm the validity of the above mentioned mechanisms derived from the apparent activation energy values, different mathematical models for heterogeneous gas–solid reactions derived by Szekely *et al.*[25,26] were applied. The mathematical formulation for gaseous diffusion,

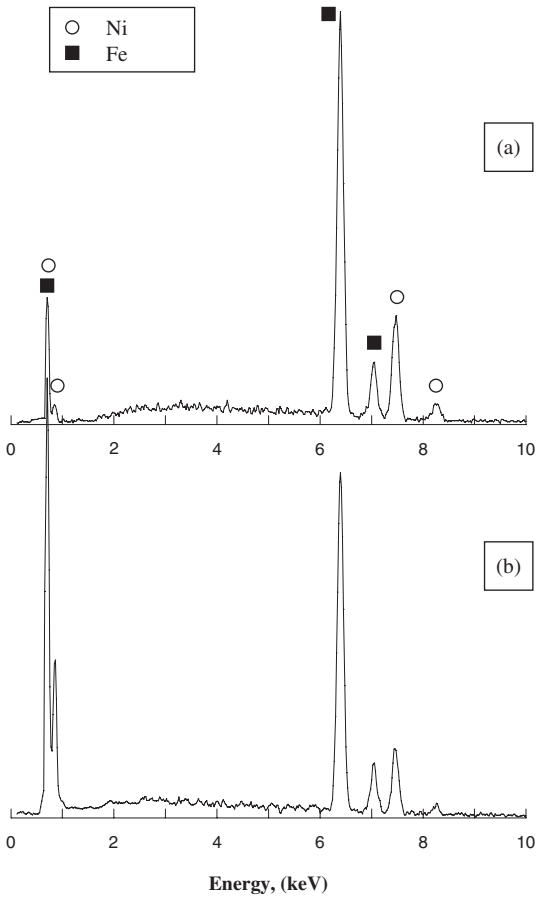

Fig. 9 EDX analysis of NiO/Fe_2O_3 samples reduced at 650°C with pure hydrogen gas. (a) 1 : 1 and (b) 1 : 2 ratios.

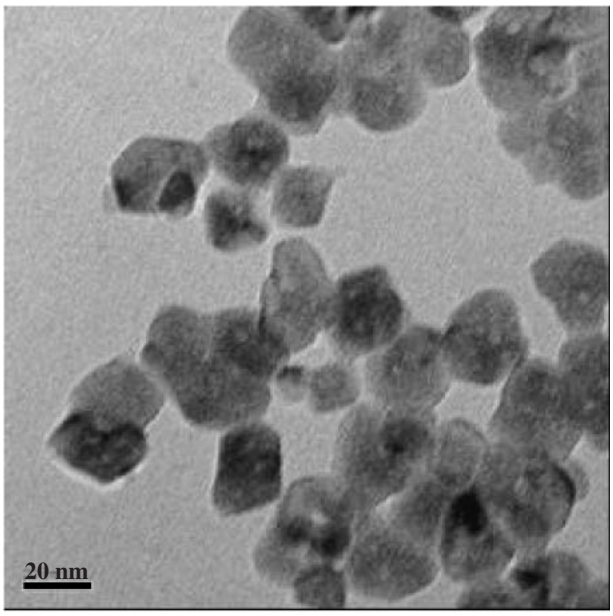

Fig. 11 TEM observation of the synthesized nanocrystalline Fe-Ni alloy after complete reduction of 1 : 2 NiO/Fe_2O_3 at 650°C.

interfacial chemical reaction, and mixed control reaction are, respectively

$$t^* = X + (1 - X)\ln(1 - X). \quad (3)$$

$$t^* = 1 - (1 - X)^{1/2}. \quad (4)$$

$$t^* = [1 - (1 - X)^{1/2}] + \hat{\sigma}^2[X + (1 - X)\ln(1 - X)] \quad (5)$$

where t^* is dimensionless time, X is the fractional reduction degree at a given reduction time, and $\hat{\sigma}^2$ is the shrinking core reduction modulus. The testing of these three mathematical

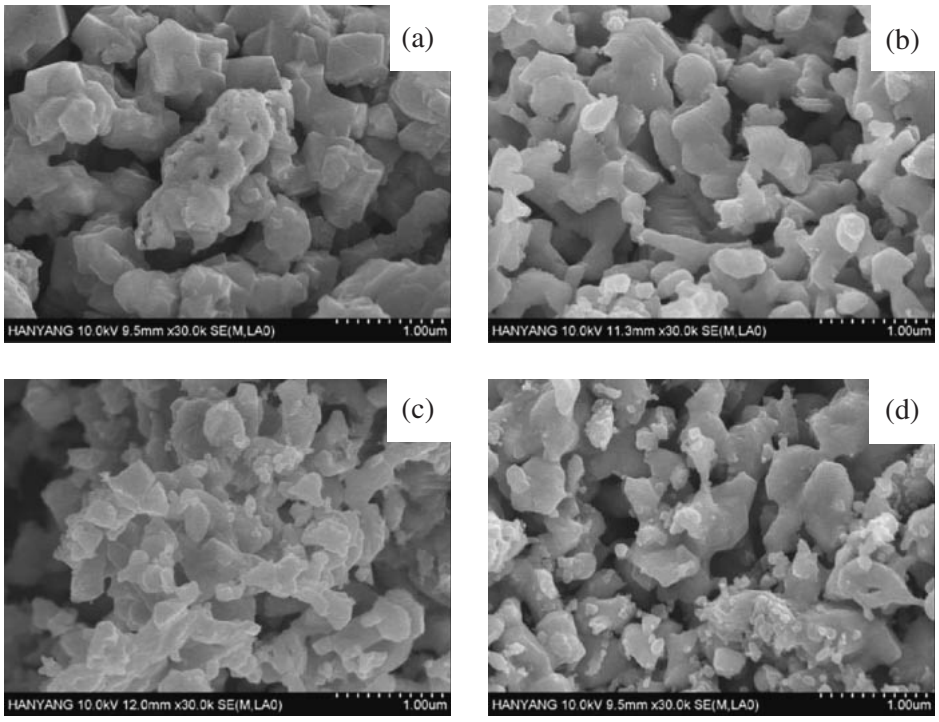

Fig. 10 SEM photos of the synthesized nanocrystalline Fe-Ni alloy after reduction of NiO/Fe_2O_3 at 550 and 650°C. (a) 1 : 1 (650°C), (b) 1 : 2 (650°C), (c) 1 : 1 (550°C), and (d) 1 : 2 (550°C).

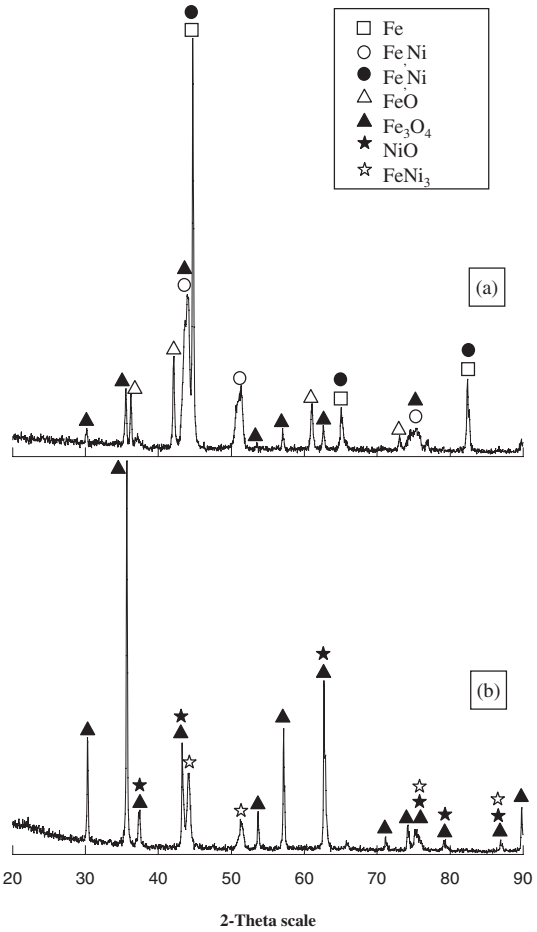

Fig. 12 XRD pattern of partially reduced 1 : 1 NiO/Fe_2O_3 at 600°C to; (a) 80% and (b) 25% reduction extent.

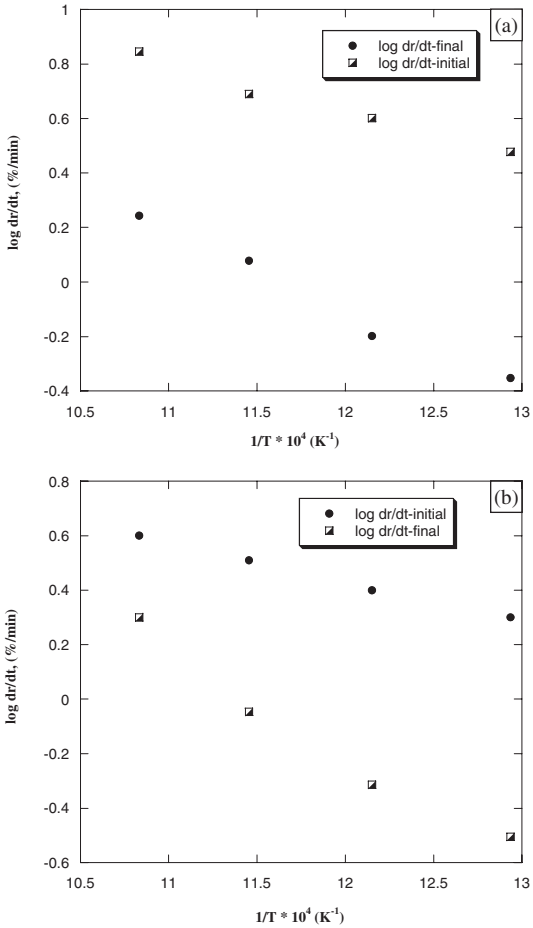

Fig. 13 Arrhenius plots for reduction of (a) 1 : 1 and (b) 1 : 2 NiO/Fe_2O_3 at the initial and final reaction stages.

formulations only resulted in a set of straight lines on the application of eq. (5) at the initial reduction stages of 1 : 1 and 1 : 2 ratios as shown in Fig. 14(a), (b) respectively. On the other hand, straight lines were obtained on the application of eq. (4) at the final reaction stages of 1 : 1 and 1 : 2 ratios as shown in Fig. 15(a) and (b) respectively. This confirmed that the reduction of NiO/Fe_2O_3 and $NiO/2Fe_2O_3$ compacts with hydrogen gas is controlled by the combined gas diffusion and interfacial chemical reaction mechanisms at the initial reaction stages while the final reaction stages is controlled by the interfacial chemical reaction mechanism.

Table 1 Relationship between activation energy values and the rate controlling step.

Activation energy value, *Ea* (KJ/mol)	Probable rate controlling step
8–16	Gas diffusion
29–42	Combined gas diffusion and interfacial chemical reaction
60–67	Interfacial chemical reaction
> 90	Solid-state diffusion

4. Conclusion

(1) Molar ratios 1 : 1 and 1 : 2 of very fine (1 μm) NiO and Fe_2O_3 were mixed and fired at 500°C for 1 h. The average crystallite size of the fired powder was 44.4 and 52 nm for 1 : 1 and 1 : 2 ratios respectively.

(2) Fired compacts were reduced in hydrogen atmosphere at 500–650°C. Complete reduction was achieved with synthesis of nanocrystalline $Fe_{1-x}Ni_x$ alloy of 33 and 20 at% Ni for 1 : 1 and 1 : 2 NiO/Fe_2O_3 ratios respectively.

(3) The crystalline sizes of the synthesized $Fe_{1-x}Ni_x$ alloy are ranged from 13–34 nm for both reduced mixture.

(4) Owing to the lower oxygen contents and higher total pore volume, reduction rate of NiO/Fe_2O_3 was faster with shorter reaction time than $NiO/2Fe_2O_3$ whereas this difference decreased sharply with increasing reduction temperatures.

(5) The calculated activation energy values from Arrhenius equation indicate that for the two different mixed oxides ratios, the reduction process at the initial reaction stages is controlled by the combined gas diffusion and interfacial chemical reaction mechanisms while the final reaction stages is controlled by the interfacial chemical reaction mechanism. The concluded mechanisms were confirmed by applying different mathematical models for heterogeneous gas–solid reactions.

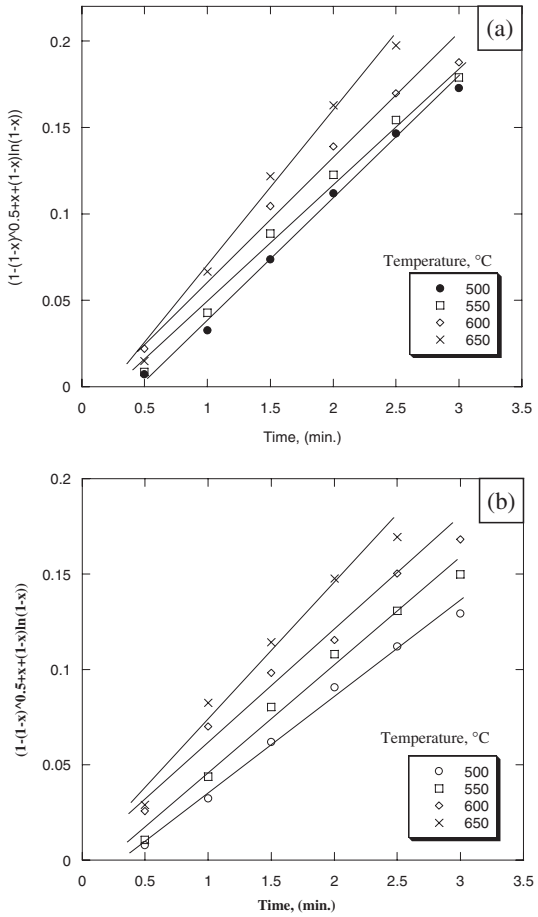

Fig. 14 Applying the mathematical formulation for the mixed control of gas diffusion and interfacial chemical reaction mechanism at the initial reduction stages of (a) 1 : 1 and (b) 1 : 2 NiO/Fe_2O_3 ratios.

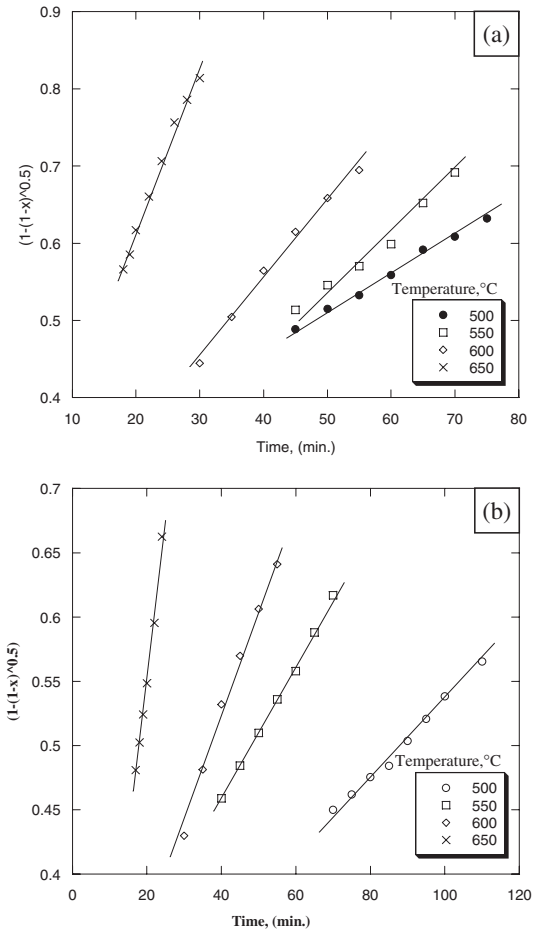

Fig. 15 Applying the mathematical formulation for the interfacial chemical reaction mechanism at the final reduction stages of (a) 1 : 1 and (b) 1 : 2 NiO/Fe_2O_3 ratios.

REFERENCES

1) Q. Liao, R. Tannenbaum and Z. Wang: J. Phys. Chem. B **110** (2006) 14262–14265.
2) W. Tremel, H. Kleinke, V. Derstroff and C. Reisner: J. Alloys Compd. **219** (1995) 73.
3) N. Grobert, M. Mayne, M. Terrones, J. Sloan, R. Kamalakaran, T. Seeger, H. Terrones, N. Ruhle, H. W. Kroto and J. Hutchison: Chem. Commun., (2001) 471.
4) A. Datta, D. Chakravorty and S. Chintalapudi: J. Magn. Magn. Mater. **205** (1999) 301.
5) H. R. Khan and K. Petrikowski: J. Magn., Mater. **249** (2002) 458.
6) J. Tang, K. Wang, L. Spinu, P. Schilling, N. Moelders and J. Hutchison: Chem. Commun. (2001) 471.
7) H.-Q. Wu, Y.-J. CaO, P.-S. Yuan, H.-Y. Xu and X.-W. Wei: Chemical Physical Letters **406** (2005) 148–153.
8) E. Jartych, J. K. Zurawicz, D. Oleszak and M. Pekala: Nanostructured Materials **12** (1999) 927.
9) X. Li, R. Gong, Y. Nie, Z. Zaho and H. He: Materials Chemistry and Physics **94** (2005) 408.
10) K. Werkmeister, F. Rullang, M. Heyer and G. Schwitzgebel: Nanostructured Materials **12** (1999) 229.
11) V. A. Ahabashov, T. M. Lapina and V. P. Pilyugin: Nanostructured Materials **9** (1997) 677.
12) R. N. Panda and N. S. Gajbhiye: J. Appl. Phys. **86** (1999) 3295.
13) K. V. P. M. Shafi and A. Gedanken: J. Appl. Phys. **81** (1997) 6901–6905.
14) E. Jartych, J. Zurawicz, D. Oleszak and M. Pekala: NanoStructured Materials **12** (1999) 927–930.
15) H.-Q. Wu, Y.-J. CaO, P.-S. Yuan, H.-Y. Xu and X.-W. Wei: Chemical Physical Letters **406** (2005) 148–153.
16) Y. Chimi, N. Ishikawa, A. Iwase and F. Ono: Nuclear Instruments and Methods in Physics Research B **257** (2007) 388–391.
17) C. Kuhrt and L. Schultz: J. Appl. Phys. **73** (1993) 1975.
18) Y. Zhou and M. Harmelin: J. Mater. Sci. Eng. A **133** (1991) 775.
19) S. Kima, H. Sohn, Y. Joo, T. Yim, H. Lee and T. Kang: Surf. Coat. Technol. **199** (2005) 43.
20) J. S. Lee, T. H. Kim, J. H. Yu and S. W. Chung: Nano-Structured Materials **9** (1997) 153–156.
21) K. S. Abdel Halim, M. Bahgat and O. A. Fouad: Material Science and Technology **22** (2006) 1396–1400.
22) S. Du, N. S. Srinivasan and L. I. Staffanson: Scand. J. Metall. **17** (1998) 226.
23) A. A. El-Geassy: Scand. J. Metall. **27** (1998) 205.
24) A. A. El-Geassy: ISIJ International **36** (1996) 1328.
25) J. Szekely, J. Evans and H. Y. Sohn: *Gas Solid Reaction*, (New York, Academic Press 1976).
26) H. Y. Sohn and J. Szekely: Chem. Eng. Sci. **27** (1972) 763.